RESEARCH ARTICLE

Key Points:
- TS07D model increases resolution given more data and basis functions
- Magnetic field data inside $4R_E$ improves the empirical picture
- New version of TS07D resolves eastward and banana currents

Empirical modeling of the storm time innermost magnetosphere using Van Allen Probes and THEMIS data: Eastward and banana currents

G. K. Stephens[1], M. I. Sitnov[1], A. Y. Ukhorskiy[1], E. C. Roelof[1], N. A. Tsyganenko[2], and G. Le[3]

[1]The Johns Hopkins University Applied Physics Laboratory, Laurel, Maryland, USA, [2]Institute and Faculty of Physics, Saint-Petersburg State University, Saint-Petersburg, Russia, [3]NASA Goddard Space Flight Center, Greenbelt, Maryland, USA

Abstract The structure of storm time currents in the inner magnetosphere, including its innermost region inside $4R_E$, is studied for the first time using a modification of the empirical geomagnetic field model TS07D and new data from Van Allen Probes and Time History of Events and Macroscale Interactions during Substorms missions. It is shown that the model, which uses basis-function expansions instead of ad hoc current modules to approximate the magnetic field, consistently improves its resolution and magnetic field reconstruction with the increase of the number of basis functions and resolves the spatial structure and evolution of the innermost eastward current. This includes a connection between the westward ring current flowing largely at $R \gtrsim 3R_E$ and the eastward ring current concentrated at $R \lesssim 3R_E$ resulting in a vortex current pattern. A similar pattern coined 'banana current' was previously inferred from the pressure distributions based on the energetic neutral atom imaging and first-principles ring current simulations. The morphology of the equatorial currents is dependent on storm phase. During the main phase, it is complex, with several asymmetries forming banana currents. Near *SYM-H* minimum, the banana current is strongest, is localized in the evening-midnight sector, and is more structured compared to the main phase. It then weakens during the recovery phase resulting in the equatorial currents to become mostly azimuthally symmetric.

1. Introduction

Direct statistical investigations of the magnetic field [*Le et al.*, 2004; *Jorgensen et al.*, 2004] and particle fluxes [e.g., *Lui*, 2003; *Roelof et al.*, 2004], as well as first-principles ring current simulations [*Fok et al.*, 1993; *Liemohn et al.*, 2001; *Zaharia et al.*, 2006], and empirical geomagnetic field models [*Tsyganenko et al.*, 2003; *Sitnov et al.*, 2008] show that the spatial distribution of magnetospheric currents is highly variable during geomagnetic storms developing strong noon-midnight and dawn-dusk asymmetries. However, the progress in reconstructing the dynamics and morphology of storm time magnetospheric currents remains limited in each case. For example, statistical studies based on binning data in the *Dst* index value effectively mix main and recovery phases of storms since the sign of the derivative of the *Dst* index was not included. The first-principles ring current simulations are not global and rely on the external boundary conditions (e.g., at geosynchronous orbit) to describe ring current particle drifts as well as on ad hoc magnetic field models with the sources outside of the model boundary that cannot be described self-consistently. Empirical geomagnetic field models were inherently limited until recently [*Tsyganenko*, 2002a, 2002b] because of a small number of ad hoc custom-tailored modules comprising the model and making it difficult to separate the actual structure of magnetospheric currents from artifacts imposed by the model architecture. To overcome the latter limitation *Tsyganenko and Sitnov* [2007] proposed a new approach, in which the custom-tailored modules for all equatorial currents were replaced by regular basis function expansions. The new approach made the empirical modeling less dependent on the ad hoc assumptions built in the model structure as well as extensible, that is, providing higher resolution as long as more data sets become available.

The new approach was used in the empirical model TS07D, which has been applied to storms driven by coronal mass injections (CME) [*Sitnov et al.*, 2008] and corotating interaction regions (CIR) [*Sitnov et al.*, 2010] as well as to long duration steady magnetospheric convection events (SMC) [*Stephens et al.*, 2013]. The model

revealed interesting new features in storm time currents such as the hook- and belt-shaped currents in CME- and CIR-driven storms, respectively, as well as two drastically different SMC regimes characterized by the near-Earth minimum and extended plateau in the radial profile of the equatorial magnetic field. However, the model's capability to increase the resolution given more data has never been shown before. Moreover, being limited by the data sets outside $\sim 4R_E$ [*Sitnov et al.*, 2008], TS07D did not resolve the eastward current flowing at $R \lesssim 3R_E$, which is key in the description of the pressure-driven currents near the equatorial plane [*McEntire et al.*, 1985; *Lui et al.*, 1987; *Roelof*, 1989; *Roelof et al.*, 2004].

In this work we investigate the innermost magnetosphere by means of a modified version of the TS07D model. It uses a new database, combining magnetometer data from the original TS07D database in addition to new data from the Van Allen Probes and THEMIS missions, which now includes the innermost region of the magnetosphere inside $\sim 4R_E$. We also increase the number of the equatorial basis functions from 45 up to 260 and show how it improves the model validation results. Further, we show that given enough data, the new model successfully reconstructs the eastward current, including its local time variations during the March 2013 magnetic storm.

2. Description of Model

The TS07D empirical magnetic field model [*Tsyganenko and Sitnov*, 2007; *Sitnov et al.*, 2008] employs a fundamentally different description of the equatorial current systems compared to classical empirical models [*Tsyganenko*, 2002a, 2002b; *Tsyganenko and Sitnov*, 2005; *Tsyganenko*, 2013, and references therein]. Traditionally, these models construct the equatorial current systems as a combination of symmetric and partial ring current modules as well as a tail current module. With the ever growing abundance of in situ magnetometer data, it has become possible to instead represent the equatorial fields using a series expansion, i.e., a linear combination of basis functions, which must describe an arbitrary distribution of currents in the equatorial plane while obeying the Gauss's law for magnetism and Ampère's law. As is shown by *Tsyganenko and Sitnov* [2007], the resulting magnetic field can be represented in the form

$$\boldsymbol{B}(\rho, \phi, z) = \sum_{n=1}^{N} a_{0n}^{(s)} \boldsymbol{B}_{0n}^{(s)} + \sum_{m=1}^{M} \sum_{n=1}^{N} a_{mn}^{(o)} \boldsymbol{B}_{mn}^{(o)} + \sum_{m=1}^{M} \sum_{n=1}^{N} a_{mn}^{(e)} \boldsymbol{B}_{mn}^{(e)} \tag{1}$$

where $\{\rho, \phi, z\}$ is a cylindrical coordinate system with the Z axis is along the dipole axis, $\boldsymbol{B}_{\alpha\beta}^{(\gamma)}$ are the basis functions, and $a_{\alpha\beta}^{(\gamma)}$ are scaling coefficients in the expansion. N and M are integer parameters, which determine the number of radial (ρ) and azimuthal (ϕ) expansions, respectively. The set of functions $\boldsymbol{B}_{\alpha\beta}^{(\gamma)}$ is built on the general solution of Ampère's equation for an infinitely thin equatorial current layer that can be obtained by the separation of variables method. These solutions are naturally split into azimuthally symmetric modes denoted by the index (s) and two families of asymmetric solutions, (o) and (e), having factors $\sin(m\phi)$ and $\cos(m\phi)$ with $m \geq 1$ in their vector-potential representation and corresponding to its odd and even parity components with respect to the plane $y = 0$. The original solutions of the Ampère's equation are then generalized to assume the finite half thickness D of the equatorial current sheet. Although the model has an option of varying the parameter D in the equatorial (X, Y) plane, here we assume a constant spatial thickness that may vary as function of time and activity level. An example of such a function corresponding to the first term in (1) can be expressed through the azimuthal component of the vector potential $\left(A_\phi\right)_{0n}^{(s)}(k, \rho, z) = J_1(k_n\rho) \exp\left(-k_n\sqrt{z^2 + D^2}\right)$ where J_1 is the Bessel function of the first order, $k_n = n/\rho_0$, and ρ_0 is the radial scale, corresponding to the largest wavelength in the radial expansion. The full expression for (1) is formulated in equations 14–17 in *Tsyganenko and Sitnov* [2007] including example plots of the resultant equatorial electric current flow lines in Figure 1 in the aforementioned work. Note that in contrast to the other free parameters of the model, such as the scaling coefficients $a_{\alpha\beta}^{(\gamma)}$ and current sheet thickness D, the parameters ρ_0, N, and M are fixed as they determine the adopted resolution of the model. Furthermore, every current element in the sum (1) is shielded using a similar expansion for the magnetic field of the magnetopause currents as described in more detail in [*Tsyganenko and Sitnov*, 2007]. The result is an expression for the equatorial currents that has no predefined structure, allowing the modeled current distribution to be driven only by the magnetometer data. This naturally allows for the reconstruction of asymmetries in the ring current that may dominate the global structure of the magnetosphere during storm times.

An advantage to the basis function expansion approach is that by increasing the number of terms M and N in (1) with a fixed radial scale ρ_0, arbitrary spatial resolution can be achieved bounded only by the necessity
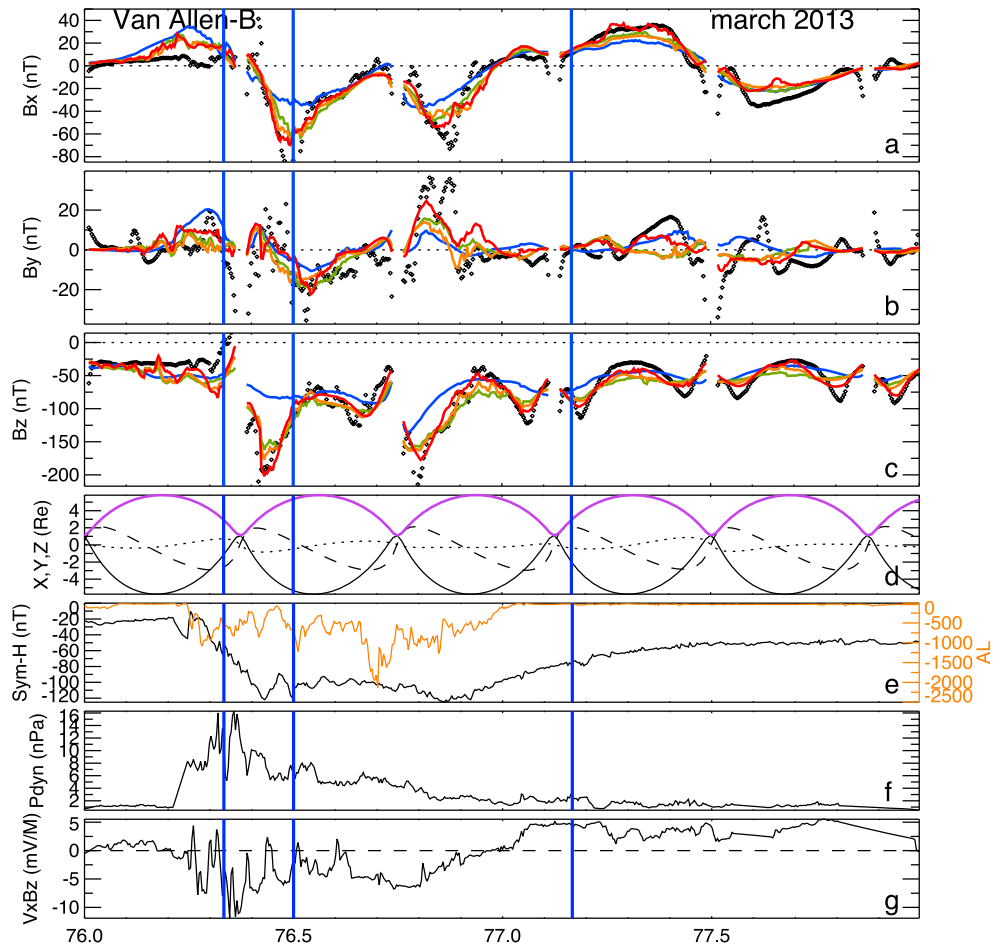
Figure 1. The validation of the empirical magnetic field model for the March 2013 geomagnetic storm using Van Allen Probe-B magnetometer data. (a, b, and c) The temporal evolution of the (a) B_x, (b) B_y, and (c) B_z components of the external magnetic field as measured by Van Allen Probe-B in black diamonds, with the original resolution model ($M = 4$, $N = 5$) fit to the original database output in blue, the original resolution model ($M = 4$, $N = 5$) fit to the Van Allen Probes database output in green, the enhanced resolution model ($M = 6$, $N = 8$) fit to the Van Allen Probes database output in orange, and the enhanced resolution ($M = 6$, $N = 20$) model fit to the Van Allen Probe database output in red. (d) The Van Allen Probe-B x (solid line), y (dashed line), and z (dotted line) GSM ephemeris components and the radial distance (purple line). (e) The pressure-corrected storm index SYM-H^* (black line) and substorm index AL (orange line). (f and g) The solar wind dynamic pressure and electric field from the OMNI database. The moments of interest (day 17/DOY 76, UT 08:00, day 17/DOY 76, UT 12:00, and day 18/DOY 77, UT 04:00) are represented as the vertical blue lines.

of proper magnetometer data coverage to constrain the model. The azimuthal resolution is controlled by the number of terms M while N governs the radial resolution. In this study we use $\rho_0 = 20R_E$ and three radial and azimuthal sets of basis functions: Set 1 with $(N, M = (5, 4)$, Set 2 with $(N, M) = (8, 6)$, and Set 3 with $(N, M) = (20, 6)$. This results in a total of 45, 104, and 260 scaling coefficients in the equatorial expansion in (1), respectively. The solar wind dynamic pressure is incorporated into the equatorial current system by replacing the scaling coefficient $a_{\alpha\beta}^{(\gamma)}$ with two scaling coefficients, one of which is a function of the dynamic pressure $(a_{0,\alpha\beta}^{(\gamma)} + a_{1,\alpha\beta}^{(\gamma)} \sqrt{P_{dyn}})$, doubling the number of scaling coefficients to 90, 208, and 520, respectively. Set 1 was used in the original version of TS07D and the corresponding studies of the storm time magnetosphere [*Sitnov et al.*, 2008, 2010; *Stephens et al.*, 2013]. Below, we show that Sets 2 and 3 given the sufficient number of data points in the model database provide progressively higher resolution in space and resolve interesting new features in the storm time morphology of the innermost magnetospheric currents. The number of radial expansions $N = 20$ for Set 3 was chosen to match the radial scale $\rho_0 = 20R_E$, resulting in one radial expansion per Earth radii. Similarly, the number of azimuthal expansions $M = 6$, which corresponds to 12 expansions

since both even and odd symmetry are included, results in one azimuthal expansion per 30°, yielding approximately one expansion per square R_E in the inner boundary of the eastward current region ($R \approx 1.7R_E$). Set 2 is between the two resolutions and is meant to demonstrate the effect of increasing the number of radial expansions.

Other details of TS07D structure, including effects of the dipole tilt, tail current sheet warping, and twisting can be found in *Tsyganenko and Sitnov* [2007] and *Sitnov et al.* [2008]. Here we only discuss another major group of magnetospheric currents distinct from the equatorial system (1). Termed field aligned currents (FACs) because close to Earth they follow the magnetic field lines, these currents connect the equatorial system of currents with the ionosphere and the latter with the magnetopause. The FAC module describes the magnetic field of currents flowing into and out of the ionosphere along two deformed conical layers corresponding to region 1 and region 2 current systems [*Tsyganenko*, 2002a]. The size of each system is an adjustable parameter, while the azimuthal distribution of inflowing and outflowing currents is controlled by the relative contributions of two groups of basis functions with odd and even symmetry due to factors $\sin(k\phi)$ and $\cos(k\phi)$, respectively, where k is a positive integer number. The first group represents the main ("antisymmetric") part of the FAC system, in which the duskside currents have the same magnitude but opposite direction to those at dawn, while the second group has an even (or "symmetric") distribution of currents with respect to the noon-midnight meridian plane, which allows one to model the azimuthal rotation of the original antisymmetric distribution of FACs. This study follows the approach of the previous works in that the region 1 currents utilize the first and second harmonics ($k = 1, 2$) but only the odd ($\sin(k\phi)$) symmetry, while the region 2 currents use only the first harmonic ($k = 1$) but both the odd ($\sin(k\phi)$) and even ($\cos(k\phi)$) symmetry allowing for the rotation of the region 2 FAC. Such a description is rather simplistic, and it does not take into account in particular the almost continuous transition between region 1 and region 2 current systems, including a differential rotation of those currents with latitude and resulting in the Harang discontinuity effect [e.g., *Erickson et al.*, 1991]. However, it appears to be quite sufficient for the description of the expected morphology of the innermost magnetosphere currents. In particular, as is shown by *Roelof et al.* [2004], the closure between the eastward and westward ring currents represents a low-latitude counterpart of the conventional region 2 current coupled with the westward part of the partial ring current, and it does not require any special FAC module linking the eastward current with the ionosphere.

3. Data Mining Algorithm and New Model Database

A magnetometer database with sufficient radial and local time coverage is necessary to properly fit and constrain the updated model with enhanced spatial resolution in the inner magnetosphere. The original TS07D used $\sim 10^6$ magnetospheric data points with either 5 or 15 min resolution as well as the concurrent solar wind and interplanetary magnetic field (IMF) data for the period 1995-2005 from missions Geotail, Polar, Cluster, ACE, Wind, IMP-8, GOES 8, 9, 10, and 12. However, the data coverage in space was largely limited to the region $R \gtrsim 4R_E$ ($R \gtrsim 3.2R_E$ in case of Polar). The database has been further extended due to recent spacecraft measurements inside geosynchronous orbit from the five Time History of Events and Macroscale Interactions during Substorms (THEMIS) and the Van Allen Probes (hereafter VA Probes) with the total number of data points $L_{DB} = 2,545,727$. As with the original TS07D Polar data, high-altitude ($R \geq 5R_E$) data were averaged to 15 min, and low-altitude data ($R < 5R_E$) were averaged to 5 min. Additionally, the new data sets were filtered to only include data within the *Shue et al.* [1998] modeled magnetopause. Due to the nature of least squares fitting, large deviations between the model and the magnetometer data can have large impacts on the fit. Therefore, the database only includes data where $R \geq 1.5R_E$ and THEMIS data with $B_{ext} \geq 200$ nT has been removed, where B_{ext} is the external magnetic field, i.e., the magnetic field without the main International Geomagnetic Reference Field field. The THEMIS data filtering was necessary, as the data would occasionally contain magnetometer measurements that were on the order of 1000 nT difference from the model. For future studies, a more thorough cleaning of the data should be performed, where magnetopause crossings and anomalous data records are removed through visual inspection. More details of the new database are provided in Table 1.

A dynamical binning method called nearest neighbors is utilized to select a small subset of the whole magnetometer database used to fit the model. A global parameter space is formed by the solar wind electric field parameter averaged over substorm scales $\langle vB_z \rangle$, similarly averaged storm activity index $\langle SYM\text{-}H^* \rangle$, and its averaged time derivative $D\langle SYM\text{-}H^* \rangle / Dt$ (for detail see *Sitnov et al.* [2008]) obtained from the original 5 min

Table 1. Summary of Magnetospheric Data

Spacecraft	Data Points	% of Total	Data Points Within VAP's Apogee	% Within VAP's Apogee	Period
Cluster	65,735	2.58	10,541	1.21	2001 — 2005
Geotail	135,446	5.32	0	0.00	1995 — 2005
Polar	316,747	12.44	126,624	14.50	1996 — 2005
IMP-8	16,317	0.64	0	0.00	1995 — 2005
GOES-08	233,674	9.18	0	0.00	1995 — 2003
GOES-09	84,951	3.34	0	0.00	1995 — 1998
GOES-10	213,295	8.38	0	0.00	1999 — 2005
GOES-12	79,569	3.13	0	0.00	2003 — 2005
THEMIS-A	322,286	12.66	125,055	14.32	2007 — 2015
THEMIS-B	33,562	1.32	12,408	1.42	2007 — 2011
THEMIS-C	68,757	2.70	20,923	2.40	2007 — 2011
THEMIS-D	323,963	12.73	126,648	14.50	2007 — 2015
THEMIS-E	327,527	12.87	127,402	14.59	2007 — 2015
VA-A	162,442	6.38	162,442	18.60	2012 — 2015
VA-B	161,456	6.34	161,456	18.48	2012 — 2015

averaged solar wind and *SYM-H* data. The *SYM-H* data have been pressure corrected (following *Tsyganenko* [1996] where $SYM\text{-}H^* = 8.0 SYM\text{-}H - 13.0\sqrt{P_{dyn}}$), and the solar wind data have been linearly interpolated across gaps. These parameters are then normalized by their standard deviation and evaluated at a 5 min cadence for the period covering the magnetometer database 1995 to the spring of 2015, thus forming a collection of points in the 3-D parameter space. For each modeled moment, corresponding to a point in the 3-D parameter space, the nearest L_{NN} neighboring points based on their Cartesian distance are selected, which are then organized into contiguous time intervals. These intervals are overlapped with the magnetometer database forming a collection of magnetic field measurements from times that are most similar to the moment of interest, from which the model is fit using least squares regression. A weight is applied to each $0.5 R_E$ bin to approximately normalize each bin's impact on the fit, which is detailed in *Tsyganenko and Sitnov* [2007]. The number $L_{NN} \ll L_{DB}$ of such points called the nearest neighbors (NN) [*Sitnov et al.*, 2008] must nevertheless be large enough to provide a dense coverage of the considered magnetospheric region. Following the earlier TS07D studies the number of NNs is $L_{NN} = 8000$.

4. Model Validation and Flexibility Tests

The new model with enhanced spatial resolution and innermost magnetosphere data coverage has been applied for the empirical reconstruction of the March 2013 storm. This was one of the first sizable storms of the Van Allen Probes era [e.g., *Gkioulidou et al.*, 2014]. The storm was caused by a coronal mass ejection [*Baker et al.*, 2014] that arrived at the magnetosphere around 0600 UT on 17 March (DOY 76) and reached a *SYM*-H minimum of -132 nT later in the day at 2028 UT. The solar wind interplanetary magnetic field gradually turned northward by around 0000 UT on 18 March (DOY 77), after which substorm activity abruptly ceased as indicated by the *AL* index. Figure 1 displays the solar wind conditions for this storm.

This storm offers an opportunity to check the flexibility of the enhanced resolution versions of TS07D, including its expected improvement with the increase of the number of the equatorial basis functions. To accomplish this, we have tested the TS07D model at three resolutions: the original resolution, Set 1 with $(N, M) = (5, 4)$, and two enhanced resolutions, Set 2 with $(N, M) = (8, 6)$, and Set 3 with $(N, M) = (20, 6)$. For simplicity, these models were fit to only the VA Probes magnetometer data with the total number of points $L_{DB}^{(VA)} = 323,898$. Since there are only several storms during the VA Probes era, the model fit will be strongly dominated by data for the considered storm making the empirical reconstruction procedure in this resolution experiment closer to event-oriented models [e.g., *Kubyshkina et al.*, 1999]. For this storm, the typical number of magnetometer measurements included in each fit is on the order of 1000 – 1500. This is a smaller number than in the previous TS07D studies since the VA Probes database covers mid-2012 through spring of
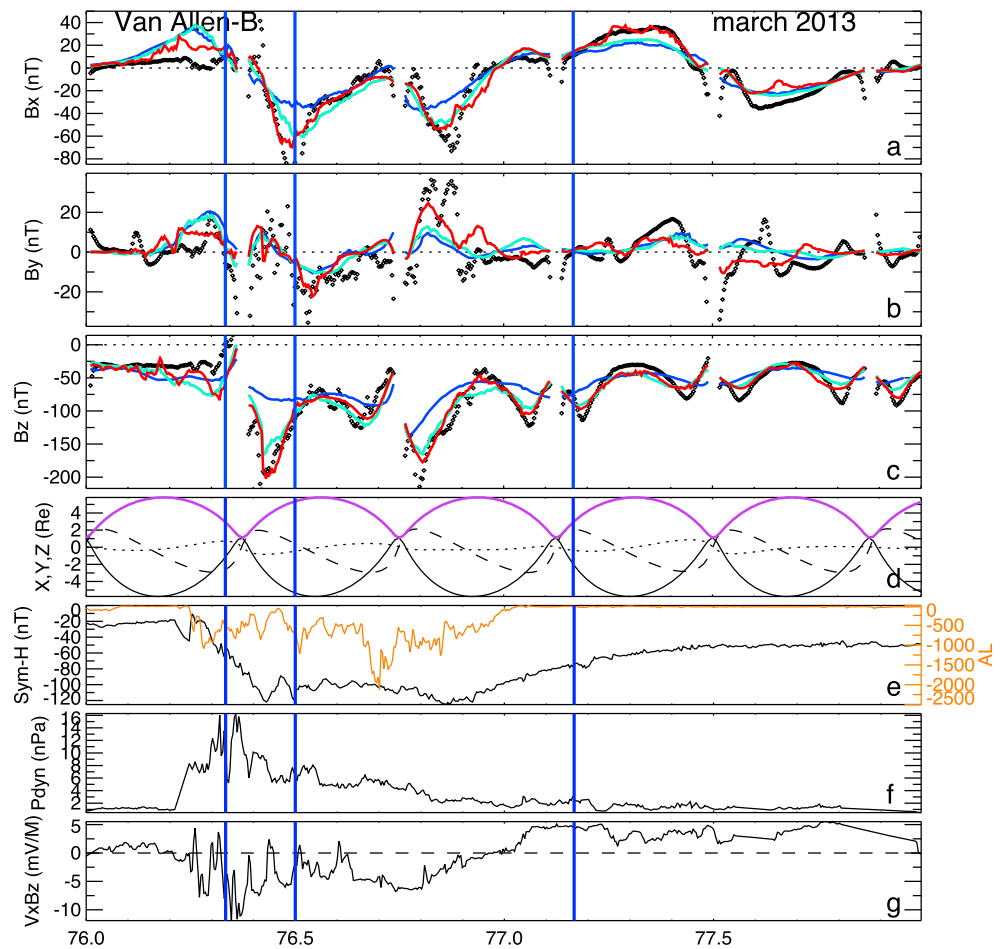
Figure 2. The validation of the empirical magnetic field model for the March 2013 geomagnetic storm using Van Allen Probe-B magnetometer data. The panels are the same as Figure 1, except (a, b, and c) show the temporal evolution of the (a) B_x, (b) B_y, and (c) B_z components of the external magnetic field using the original resolution ($M = 4$, $N = 5$) model's output in blue, the enhanced resolution ($M = 6$, $N = 20$) model fit to the Van Allen Probe database output in red, and the enhanced resolution ($M = 6$, $N = 20$) model fit to a composite database of the original TS07D database in addition to the THEMIS and Van Allen Probe database output in cyan. The latter version of the model is used in the proceeding plots.

2015 while the parameter space used for identifying nearest neighbors spans the entire database from 1995 through the spring of 2015. This may not be enough data to sufficiently reconstruct the global shape of the magnetosphere, but here we are only demonstrating the model's capability to reconstruct smaller-scale features in the inner magnetosphere as the number of expansions is increased. The model output is validated against the VA Probe-B measurements during the storm and is displayed in Figures 1a–1c, along with the output of the original TS07D model ((N, M) = (5, 4) and the original database). The original TS07D modeled field (blue line) reveals substantial deviations from the VA Probe-B data (black diamonds). This is to be expected as the original database excluded data within $R \lesssim 3.2 R_E$. Sets 1, 2, and 3 are overplotted by green, orange, and red lines, respectively. As the number of expansions is increased, the model can more accurately reconstruct the small spatial structures in the magnetic field measurements that exist in the inner magnetosphere. The remaining discrepancies of the highest-spatial resolution model based on Set 3 are still seen prior to the onset of the storm (around day 17/DOY = 76, UT 06:00) for all magnetic field components. This is caused by a gap in solar wind pressure measurements. We linearly interpolate across gaps, and in this case, the linear interpolation overestimates the dynamic pressure, causing an overcorrection in the pressure correction of *SYM-H*, resulting in an unphysical dip in SYM-H* just prior to the storm. In addition, there are deviations of ~10 nT in the B_y component that are particularly present during the recovery phase of the storm. They are most probably caused by the IMF B_y magnetic field, which is not included in the present binning of the parameter space.
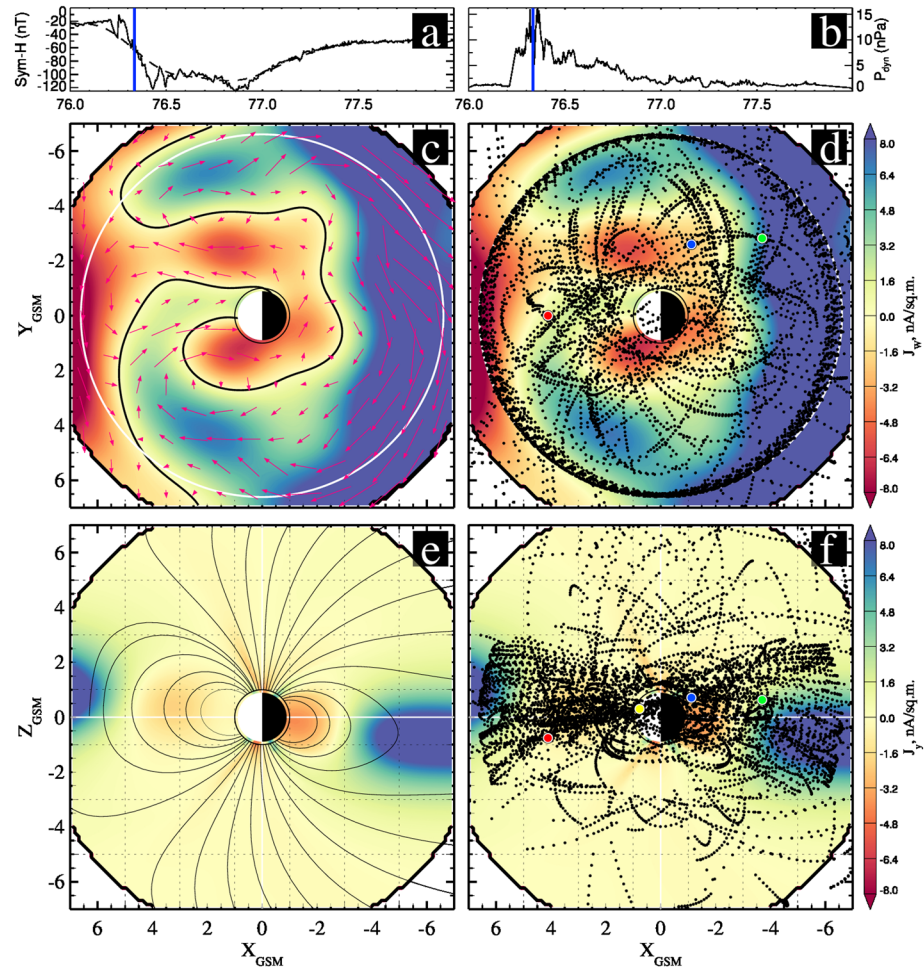
Figure 3. Reconstruction of the current density using the empirical magnetic field model for the main phase of the March 2013 geomagnetic storm (day 17/DOY 76, UT 08:00), corresponding to the left vertical blue line in Figures 1 and 2. (a and b) The pressure-corrected storm index SYM-H^* and dynamic pressure along with a blue vertical line representing the moment of interest. (c and d) The azimuthal component of the equatorial current density, with green blue representing the westward current and orange red representing eastward currents, with geosynchronous orbit being shown as a white circle. Arrows representing the projection of current density vectors are overplotted in Figure 3c along with the zero azimuthal current density contour in black. (e and f) The $+Y$ component of the current density, with blue purple representing current flowing out of the page and orange red representing current flowing into the page. Magnetic field lines are drawn on Figure 3e. The location of the spacecraft magnetometer data points (GSM) used in the fit for this moment are plotted as black circles. The locations of the spacecraft at this moment are plotted as the colored circles, showing THEMIS-A (red), THEMIS-E (yellow), VAP-A (Green), and VAP-B (Blue).

These IMF B_y-dependent effects are beyond the scope of this current work and should be addressed in later studies. Nevertheless, Figure 1 reveals consistent improvement of the model accuracy with the increase of the number of the equatorial basis functions.

Now that it has been established that increasing the number of equatorial expansions in the model can resolve smaller-scale features, we can construct a model with appropriate magnetometer coverage so that the global configuration of the electrical current morphology can be analyzed. To do this, an enhanced resolution model is constructed using Set 3 equatorial expansions and a magnetometer database consisting of the original TS07D database (Cluster, Geotail, Polar, IMP-8, GOES-08, GOES-09, GOES-10, and GOES-12) in addition to the THEMIS and VA Probes databases as discussed in section 3, for a total number of points $L_{DB} = 2,545,727$. This increases the typical number of magnetometer measurements included in each fit to
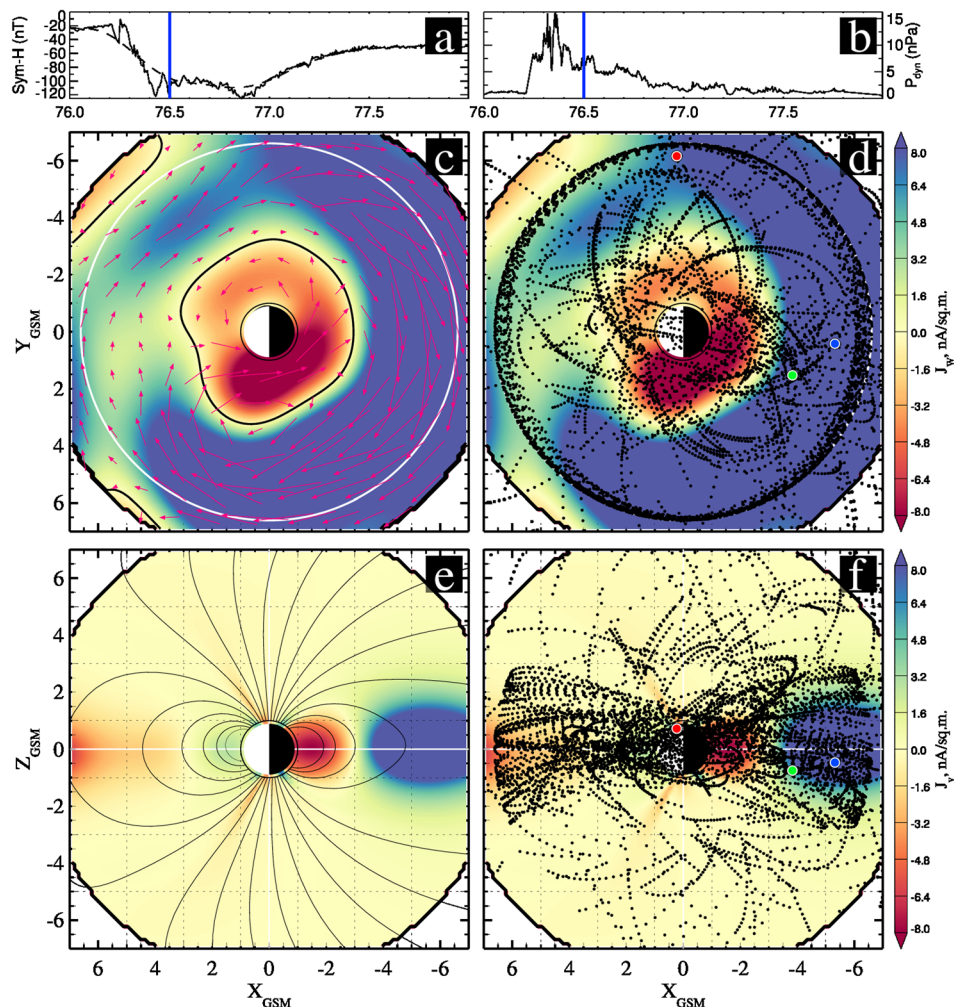
Figure 4. Reconstruction of the current density using the empirical magnetic field model nearing *SYM-H** minimum of the March 2013 geomagnetic storm (day 17/DOY 76, UT 12:00), corresponding to the center vertical blue line in Figures 1 and 2. The panels are the same as Figure 3.

8500–10,000. Similarly, this model is validated against the VA Probe-B magnetic field measurements, and the results shown in Figures 2a–2c as a cyan line. Also shown in this plot are the original TS07D model and Set 3 with the VA Probe database and as before are plotted as blue and red lines, respectively. While adding the whole database slightly worsens the validation results, presumably because the NN subset obtained from the extended database is less dominated by the present storm, they strongly improve the data coverage of the innermost magnetosphere as is seen from Figures 3, 4, and 5 (Figures 3b, 3d, 4b, 4d , 5b, and 5d), and is still significant improvement over the original TS07D model. Thus, this version of the model will be utilized in the next sections.

5. Electric Current Morphology of the Innermost Magnetosphere

Figures 3–8 display the model output for three different phases of the March 2013 storm. The first and third moments occur during similar storm disturbance levels where the pressure corrected *SYM-H* on March 17 (DOY 76) 0800 UT is -59 nT and March 18 (DOY 77) 0400 UT is -75 nT, but the first moment is during the main phase of the storm while the third is during the recovery phase. The second moment on March 17 (DOY 76) 1200 UT, Figure 4, occurs during the end of the main phase when *SYM-H* is at a minimum. Figures 1 and 2 contain three vertical blue lines indicating these moments and the associated solar wind conditions.
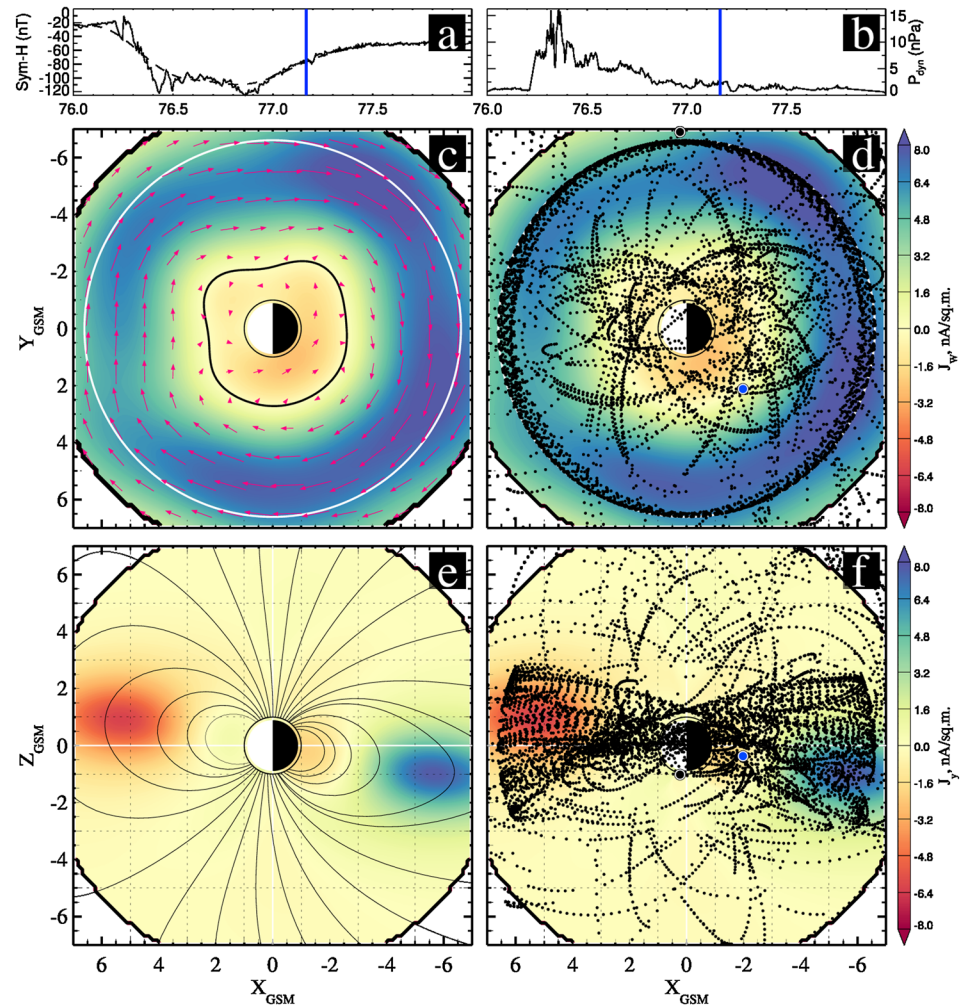
Figure 5. Reconstruction of the current density using the empirical magnetic field model for the recovery phase of the March 2013 geomagnetic storm (day 18/DOY 77, UT 04:00), corresponding to the right vertical blue line in Figures 1 and 2. The panels are the same as Figure 3.

The top color panels in Figures 3–5 show the distribution of the azimuthal component of the equatorial current density where westward flow is positive (blue) and eastward is negative (red). For the sake of visualization simplicity, the equatorial plots do not include the effects of the dipole tilt angle, $\psi = 0°$, resulting in a flat equatorial current sheet. The bottom panels in Figures 3–5 show the corresponding meridional cuts of the Y component of the current density where current flowing out of the page is positive and into the page is negative. The positions of the spacecraft used in the fit of the model are overplotted in the right color panels in Figures 3–5. Also overplotted in colored circles are the positions of the THEMIS and VA spacecraft at that particular moment.

Figures 6–8 display a 3-D visualization of the electric current morphology, including a slice of the current density in the equatorial plane that matches the top color panels in Figures 3–5. A sphere is drawn representing the Earth, and the amplitude of the FAC current systems is plotted on it showing the outward flowing currents in red and inward flowing currents in blue. The overly structured FAC pattern is a result of the rigidity of the present FAC module. Electric current lines representing the flow of the region 2 FAC are traced to display the interaction between the region 2 FAC and the equatorial currents. The lines begin at a distance of $R = 1.1R_E$ and at 9° longitude steps. The value of the latitude was chosen to match the extrema in the field aligned current density. Additional electric current lines are drawn on and above the equatorial plane ($Z = 0, 0.5R_E$) on an evenly spaced (X, Y) grid with values of -3.0, -1.5, 0.0, 1.5, and 3.0 R_E, as is shown in supporting
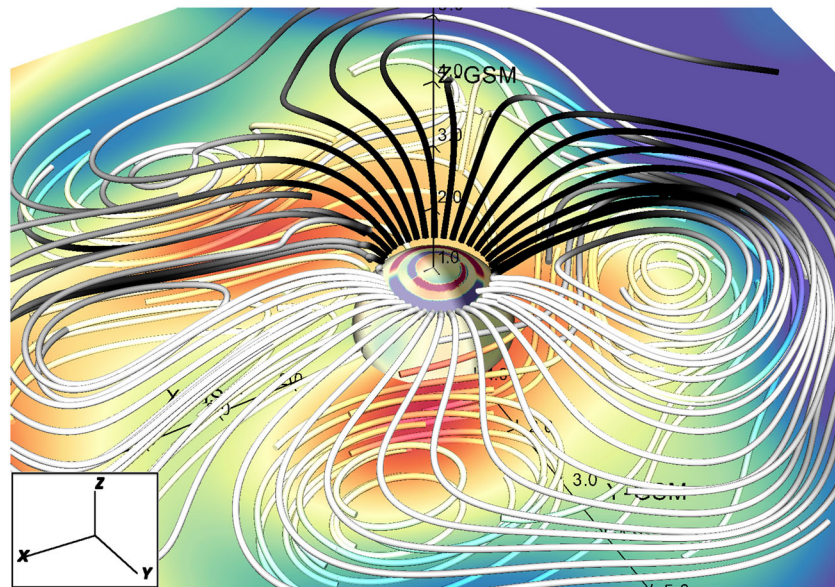
Figure 6. A three-dimensional visualization of the equatorial currents and region 2 field-aligned currents as reconstructed by the empirical magnetic field model for the main phase of the March 2013 geomagnetic storm (day 17/DOY 76, UT 08:00) corresponding to the left vertical blue line in Figures 1 and 2. The equatorial slice of the azimuthal current density matching panels (a and b) in Figure 3 is shown. The magnitude of the Birkeland current systems are plotted on a sphere representing the Earth, with outflowing electric current in red and in flowing electric current in blue. Flow lines of electric current are drawn every 9° of longitude, where white indicates current flowing into the ionosphere and black indicating current flowing out of the ionosphere. Electric current lines are also drawn on and above the equatorial plane illustrating the flow of the equatorial current systems, again with blue purple representing the westward current and orange red representing eastward current.

information Figure S1. These lines were traced both forward and backward and the color matches the azimuthal current density scale used in the top color panels in Figures 3 – 5.

During the main phase of the storm (Figures 3 and 6) the equatorial currents are complex, with the asymmetric ring current dominating the symmetric ring current. The westward ring current is completely broken around prenoon, the same region where current erosion has been observed during the main phase of other CME-driven storms [*Sitnov et al.*, 2008]. Also, just inside geosynchronous orbit in the midnight and postmidnight sector, the divergence of the overplotted current density vector arrows in Figure 3c indicates a rather strong current flowing from the ionosphere. Most of this current appears to close through the duskside magnetopause and the region 2 current flowing to the ionosphere. However, some continues to flow in the equatorial plane beyond the terminator and closes through the eastward ring current indicated by the arrows in the postnoon sector. This leads to the formation of a closed current system contained within the noon-dusk sector, or banana current [*Liemohn et al.*, 2013], which is clearly illustrated by the electric current lines in Figure 6. It is conceivable that the closure path of this feature might be a low-latitude field-aligned type current (region 3) that closes through the ionosphere. However, Figure 9, which shows 10 min of AMPERE data [*Anderson et al.*, 2014, and references therein] from (day 17/DOY 76, UT 08:00 – 08:10) including the magnetic field perturbations in the left panel and the resulting fit FAC current distributions in the right panel, shows no signature of a special low-latitude FAC system corresponding to an eastward current in the innermost magnetosphere. There is also a significant eastward current on the dayside near geosynchronous orbit. During this time the dayside magnetosphere is compressed. The *Shue et al.* [1998] standoff distance is about at geosynchronous orbit ($R_{Shue} = 6.7R_E$). Thus, the observed eastward current may well be a magnetopause current system similar to the one discussed by *Le et al.* [2004] and shown in their Figures 7d and 8d. Figure 6 demonstrates that the 3-D structure of currents, including region 2 field aligned currents, in the main storm phase is also quite complex. They bifurcate resulting in only some of the current lines participating in the formation of the nightside partial ring current, which is centered about premidnight. Several of the other current lines in Figure 6 flow from prenoon to postnoon on the dayside and appear to participate in the formation of the eastward current seen in the equatorial plots near the magnetopause.
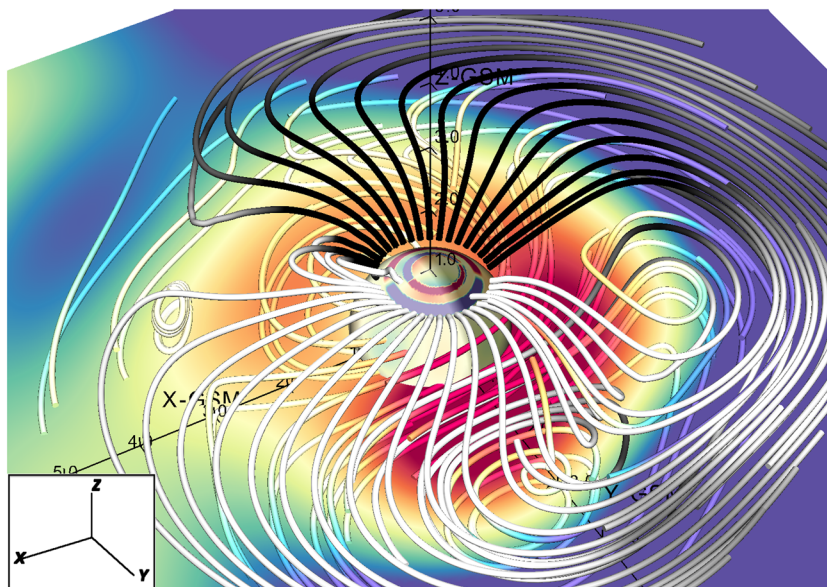
Figure 7. A three-dimensional visualization of the equatorial currents and region 2 field aligned currents as reconstructed by the empirical magnetic field model nearing *SYM-H** minimum of the March 2013 geomagnetic storm (day 17/DOY 76, UT 12:00), corresponding to the center vertical blue line in Figures 1 and 2. The details of the plot are the same as Figure 6.

The next moment farther into the storm nearing the *SYM-H** minimum (Figures 4 and 7), a larger amount (compared to the main phase) of westward ring current now makes it beyond the terminator, closing through an eastward current near dusk, forming a strong banana current in the evening-midnight sector. The erosion of the westward ring current is still observed around noon. According to Figure 4c, while the westward near-equatorial partial ring current extends over the whole nightside sector and even beyond the terminator, the eastward current is concentrated in a more limited magnetic local time (MLT) range (15 < *MLT* < 24), and it is also more confined in its radial extent. Thus, the banana involves only a small part of the westward partial ring current, most of which is closed through a region 2 FAC or the magnetopause. The region 2 current lines
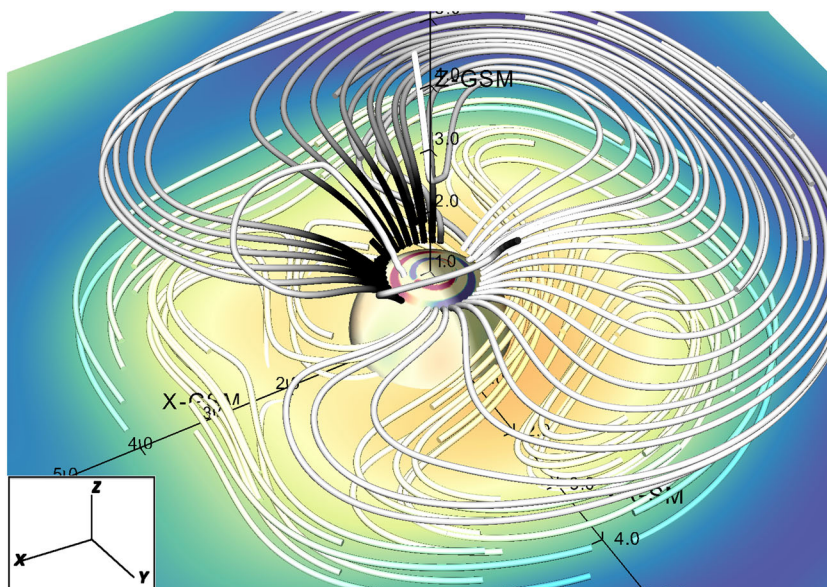

Figure 8. A three-dimensional visualization of the equatorial currents and region 2 field aligned currents as reconstructed by the empirical magnetic field model for the recovery phase of the March 2013 geomagnetic storm (day 18/DOY 77, UT 04:00), corresponding to the right vertical blue line in Figures 1 and 2. The details of the plot are the same as Figure 6.
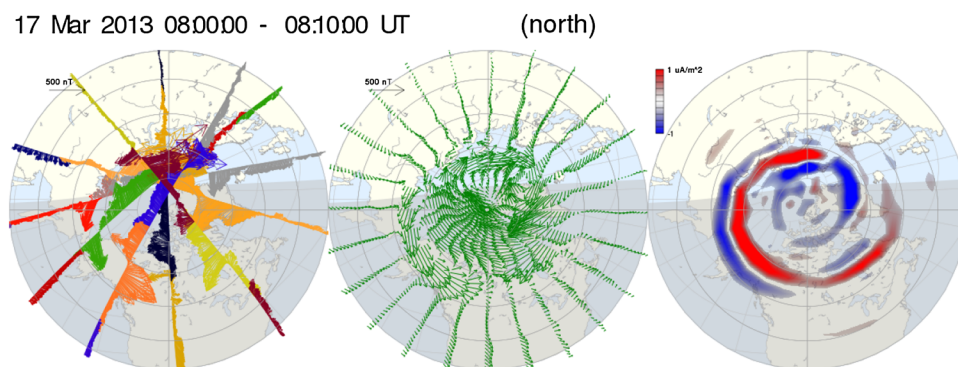
Figure 9. AMPERE data summary plots for the main phase of the March 2013 geomagnetic storm (day 17/DOY 76, UT 08:00–08:10) corresponding to the left vertical blue line in Figures 1 and 2. (left) Magnetic perturbations relative to Earth's main magnetic field; (middle) spherical cap orthogonal basis function fit to the observed magnetic perturbations; (right) resulting current distributions with upward current shown in red downward shown in blue. Gray shading in all panels indicates regions in darkness at 105 km altitude [*Anderson et al.*, 2014].

in Figure 7 are now more regular, with most of the lines helping to form a nightside partial ring current, which is still centered about premidnight.

During the recovery phase (Figures 5 and 8), both the westward and eastward become largely symmetric. The strength of the symmetric eastward current is slightly diminished in the dawn-noon sector, and along with a slight asymmetric enhancement of the westward ring current in the dusk-midnight sector forms a distinct banana current in the evening-midnight sector. The field lines have returned to a more dipolar structure. The region 2 current lines in Figure 8 become more regular, with most of the lines helping to form a weak nightside partial ring current, which is now concentrated near midnight.

The empirical picture described above is summarized in Animation S1, which represents the whole sequence of plots in the format of Figures 3–5 for two days, 17 and 18 March (DOY 76 and 77) 2013, of this storm. This animation clearly demonstrates growth and decay of the main inner magnetosphere currents. In particular, it shows the persistence of the main westward partial ring current as well as the banana current during the main phase and the extended *SYM-H* minimum period. It also shows that at later time eastward and westward currents become azimuthally symmetric and largely disconnected from each other.

6. Discussion and Conclusion

This study demonstrates the capability of the new-generation empirical models to increase their resolution given more basis functions and larger databases with increased global coverage. It also shows that the structure of the currents in the innermost magnetosphere, including the region inside $\sim 4R_E$, can be reconstructed in spite of the noisy data. The problem is that at closer distances the large absolute value of the Earth's internal magnetic field makes it difficult to differentiate between the magnetic fields from external currents and spacecraft attitude uncertainty. Nevertheless, it appears that the new data processing techniques in TS07D (e.g., singular value decomposition [*Press et al.*, 1992] used now for matrix inversion in data fitting and nearest neighbor binning) and accurate attitude reconstruction for the VA Probes [*Kirby et al.*, 2013], which utilizes a sensitive Sun sensor, provide a substantial noise reduction compared to earlier models.

The innermost magnetosphere is particularly interesting as a potential key arena for the extreme space weather events [e.g., *Ngwira et al.*, 2014]. The formation of the eastward and banana currents in this region was shown earlier based on hot plasma pressure reconstruction from energetic neutral atom imaging [*Roelof et al.*, 2004] and statistical analysis of the magnetometer data combining main and recovery phases of storms [*Le et al.*, 2004]. The concept of the eastward current providing the $j \times B$ force to balance the near-Earth decrease of the plasma pressure dates back to the earliest ring current models [*Hoffman and Bracken*, 1965]. The corresponding pressure distributions were explicitly inferred later from Active Magnetospheric Particle Tracer Explorers/Charge Composition Explorer measurements [*McEntire et al.*, 1985; *Lui et al.*, 1987; *Lui and Hamilton*, 1992]. Recently, these currents were discussed based on first-principles ring current simulations [*Liemohn et al.*, 2013]. In this study, using an advanced TS07D model, we described the data-derived eastward

and banana currents including their structure and evolution during magnetic storms. We have shown that, similar to the main (westward) ring current, the eastward ring current in the main phase is strongly asymmetric in local time and it becomes weaker and more symmetric in the recovery phase. However, the eastward ring current is even more localized in MLT compared to the westward ring current. While the asymmetry of the westward current is mainly associated with its closure through the nightside part of the region 2 FAC and the duskside magnetopause [*Sitnov et al.*, 2008], the eastward current asymmetry is due to the banana current effect. Although the banana current directly involves the westward current, its impact on the latter is relatively weak, consistent with the theoretical estimates of the ratio between eastward and westward ring currents [*Ebihara and Ejiri*, 2000]. Note that the existence of several banana-like closed current loops (corresponding to multiple pressure peaks), similar to those found in our study in the main phase and close to the *SYM-H* minimum (Figures 3, 4, 6, and 7), was predicted in ring current simulations [e.g., *Zaharia et al.*, 2005; *Chen et al.*, 2007; *Liemohn et al.*, 2013] and it is also consistent with Energetic Neutral Atoms observations of hot plasma distributions in substorms [*Baker et al.*, 2002] and storms [*Perez et al.*, 2015].

The eastward current does not have a dramatic impact on the overall shape of the magnetic field [*Lui et al.*, 1994]. However, the demonstrated capability of the advanced TS07D model to reconstruct symmetric eastward and banana currents is critically important for the use of empirical geomagnetic field models in the reconstruction of the empirical plasma pressure through the quasi-static force balance equation $\nabla p = j \times B$ [*Sergeev et al.*, 1994; *Stephens et al.*, 2013], because the position and strength of those innermost magnetosphere currents determined the upper limit of the plasma pressure buildup near Earth. The empirical storm time pressure parameter can then be used to adjust the equation of state in global MHD models [*Lyon et al.*, 2004] to advance their coupling with the ring current models [*Pembroke et al.*, 2012, and references therein].

References

Anderson, B. J., H. Korth, C. L. Waters, D. L. Green, V. G. Merkin, R. J. Barnes, and L. P. Dyrud (2014), Development of large-scale birkeland currents determined from the active magnetosphere and planetary electrodynamics response experiment, *Geophys. Res. Lett.*, 41, 3017–3025, doi:10.1002/2014GL059941.

Baker, D. N., R. E. Ergun, J. L. Burch, J.-M. Jahn, P. W. Daly, R. Friedel, G. D. Reeves, T. A. Fritz, and D. G. Mitchell (2002), A telescopic and microscopic view of a magnetospheric substorm on 31 March 2001, *Geophys. Res. Lett.*, 29(18), 1862, doi:10.1029/2001GL014491.

Baker, D. N., et al. (2014), Gradual diffusion and punctuated phase space density enhancements of highly relativistic electrons: Van Allen Probes observations, *Geophys. Res. Lett.*, 41, 1351–1358, doi:10.1002/2013GL058942.

Chen, M. W., C.-P. Wang, M. Schulz, and L. R. Lyons (2007), Solar-wind influence on MLT dependence of plasma sheet conditions and their effects on storm time ring current formation, *Geophys. Res. Lett.*, 34, L14112, doi:10.1029/2007GL030189.

Ebihara, Y., and M. Ejiri (2000), Simulation study on fundamental properties of the storm-time ring current, *J. Geophys. Res.*, 105, 15,843–15,860, doi:10.1029/1999JA900493.

Erickson, G. M., R. W. Spiro, and R. A. Wolf (1991), The physics of the Harang discontinuity, *J. Geophys. Res.*, 96(A2), 1633–1645, doi:10.1029/90JA02344.

Fok, M. C., J. U. Kozyra, A. F. Nagy, C. E. Rasmussen, and G. V. Khazanov (1993), Decay of equatorial ring current ions and associated aeronomical consequences, *J. Geophys. Res.*, 98(A11), 19,381–19,393, doi:10.1029/93JA01848.

Gkioulidou, M., A. Y. Ukhorskiy, D. G. Mitchell, T. Sotirelis, B. H. Mauk, and L. J. Lanzerotti (2014), The role of small-scale ion injections in the buildup of Earth's ring current pressure: Van allen probes observations of the 17 March 2013 storm, *J. Geophys. Res. Space Physics*, 119, 7327–7342, doi:10.1002/2014JA020096.

Hoffman, R. A., and P. A. Bracken (1965), Magnetic effects of the quiet-time proton belt, *J. Geophys. Res.*, 70, 3541–3556, doi:10.1029/JZ070i015p03541.

Jorgensen, A. M., H. E. Spence, W. J. Hughes, and H. J. Singer (2004), A statistical study of the global structure of the ring current, *J. Geophys. Res.*, 109, A12204, doi:10.1029/2003JA010090.

Kirby, K., et al. (2013), Radiation belt storm probes–Observatory and environments, *Space Sci. Rev.*, 179, 59–125, doi:10.1007/s11214-012-9949-2.

Kubyshkina, M. V., V. A. Sergeev, and T. I. Pulkkinen (1999), Hybrid input algorithm: An event-oriented magnetospheric model, *J. Geophys. Res.*, 104, 24,977–24,994, doi:10.1029/1999JA900222.

Le, G., C. Russell, and K. Takahashi (2004), Morphology of the ring current derived from magnetic field observations, *Ann. Geophys.*, 22, 1267–1295, doi:10.5194/angeo-22-1267-2004.

Liemohn, M. W., J. U. Kozyra, C. R. Clauer, and A. J. Ridley (2001), Computational analysis of the near-Earth magnetospheric current system during two-phase decay storms, *J. Geophys. Res.*, 106, 29,531–29,542, doi:10.1029/2001JA000045.

Liemohn, M. W., N. Y. Ganushkina, R. M. Katus, D. L. de Zeeuw, and D. T. Welling (2013), The magnetospheric banana current, *J. Geophys. Res. Space Physics*, 118, 1009–1021, doi:10.1002/jgra.50153.

Lui, A. T. Y. (2003), Inner magnetospheric plasma pressure distribution and its local time asymmetry, *Geophys. Res. Lett.*, 30(16), 1846, doi:10.1029/2003GL017596.

Lui, A. T. Y., and D. C. Hamilton (1992), Radial profiles of quiet time magnetospheric parameters, *J. Geophys. Res.*, 97, 19,325–19,332, doi:10.1029/92JA01539.

Lui, A. T. Y., R. W. McEntire, and S. M. Krimigis (1987), Evolution of the ring current during two geomagnetic storms, *J. Geophys. Res.*, 92, 7459–7470, doi:10.1029/JA092iA07p07459.

Lui, A. T. Y., H. E. Spence, and D. P. Stern (1994), Empirical modeling of the quiet time nightside magnetosphere, *J. Geophys. Res.*, 99, 151–157, doi:10.1029/93JA02647.

Lyon, J., J. Fedder, and C. Mobarry (2004), The Lyon–Fedder–Mobarry (LFM) global MHD magnetospheric simulation code, *J. Atmos. Sol. Terr. Phys.*, 66(15–16), 1333–1350, doi:10.1016/j.jastp.2004.03.020.

McEntire, R. W., A. T. Y. Lui, S. M. Krimigis, and E. P. Keath (1985), AMPTE/CCE energetic particle composition measurements during the September 4, 1984 magnetic storm, *Geophys. Res. Lett.*, *12*(5), 317–320, doi:10.1029/GL012i005p00317.

Ngwira, C. M., A. Pulkkinen, M. M. Kuznetsova, and A. Glocer (2014), Modeling extreme "Carrington-type" space weather events using three-dimensional global MHD simulations, *J. Geophys. Res. Space Physics*, *119*, 4456–4474, doi:10.1002/2013JA019661.

Pembroke, A., F. Toffoletto, S. Sazykin, M. Wiltberger, J. Lyon, V. Merkin, and P. Schmitt (2012), Initial results from a dynamic coupled magnetosphere-ionosphere-ring current model, *J. Geophys. Res.*, *117*, A02211, doi:10.1029/2011JA016979.

Perez, J. D., J. Goldstein, D. J. McComas, P. Valek, N. Buzulukova, M.-C. Fok, and H. J. Singer (2015), TWINS stereoscopic imaging of multiple peaks in the ring current, *J. Geophys. Res. Space Physics*, *120*, 368–383, doi:10.1002/2014JA020662.

Press, W. H., S. A. Teukolsky, W. T. Vetterling, and B. P. Flannery (1992), *Numerical Recipes in FORTRAN. The Art of Scientific Computing*, Cambridge Univ. Press, New York.

Roelof, E. C. (1989), Remote sensing of the ring current using energetic neutral atoms, *Adv. Space Res.*, *9*(12), 195–203, doi:10.1016/0273-1177(89)90329-3.

Roelof, E. C., P. C. Brandt, and D. G. Mitchell (2004), Derivation of currents and diamagnetic effects from global plasma pressure distributions obtained by IMAGE/HENA, Streamers, Slow Solar Wind, and the Dynamics of the Magnetosphere, *Adv. Space Res.*, *33*(5), 747–751, doi:10.1016/S0273-1177(03)00638-0.

Sergeev, V. A., T. I. Pulkkinen, T. I. Pellinen, and N. A. Tsyganenko (1994), Hybrid state of the tail mangetic configuration during steady convection events, *J. Geophys. Res.*, *99*, 23,571–23,582, doi:10.1029/94JA01980.

Shue, J.-H., et al. (1998), Magnetopause location under extreme solar wind conditions, *J. Geophys. Res.*, *103*, 17,691–17,700, doi:10.1029/98JA01103.

Sitnov, M. I., N. A. Tsyganenko, A. Y. Ukhorskiy, and P. C. Brandt (2008), Dynamical data-based modeling of the storm-time geomagnetic field with enhanced spatial resolution, *J. Geophys. Res.*, *113*, A07218, doi:10.1029/2007JA013003.

Sitnov, M. I., N. A. Tsyganenko, A. Y. Ukhorskiy, B. J. Anderson, H. Korth, A. T. Y. Lui, and P. C. Brandt (2010), Empirical modeling of a CIR-driven magnetic storm, *J. Geophys. Res.*, *115*, A07231, doi:10.1029/2009JA015169.

Stephens, G. K., M. I. Sitnov, J. Kissinger, N. A. Tsyganenko, R. L. McPherron, H. Korth, and B. J. Anderson (2013), Empirical reconstruction of storm time steady magnetospheric convection events, *J. Geophys. Res. Space Physics*, *118*, 6434–6456, doi:10.1002/jgra.50592.

Tsyganenko, N. A. (1996), Effects of the solar wind conditions in the global magnetospheric configurations as deduced from data-based field models (Invited), in *Proceedings of the 3rd International Conference on Substorms, Held in Versailles, 12–17 May 1996, ESA Spec. Publ.*, vol. 389, edited by E. J. Rolfe and B. Kaldeich, pp. 181–186, Eur. Space Agency, Paris.

Tsyganenko, N. A. (2002a), A model of the near magnetosphere with a dawn-dusk asymmetry 1. Mathematical structure, *J. Geophys. Res.*, *107*(A8), 1179, doi:10.1029/2001JA000219.

Tsyganenko, N. A. (2002b), A model of the near magnetosphere with a dawn-dusk asymmetry 2. Parameterization and fitting to observations, *J. Geophys. Res.*, *107*(A8), 1176, doi:10.1029/2001JA000220.

Tsyganenko, N. A. (2013), Data-based modelling of the Earth's dynamic magnetosphere: A review, *Ann. Geophys.*, *31*, 1745–1772, doi:10.5194/angeo-31-1745-2013.

Tsyganenko, N. A., and M. I. Sitnov (2005), Modeling the dynamics of the inner magnetosphere during strong geomagnetic storms, *J. Geophys. Res.*, *110*, A03208, doi:10.1029/2004JA010798.

Tsyganenko, N. A., and M. I. Sitnov (2007), Magnetospheric configurations from a high-resolution data-based magnetic field model, *J. Geophys. Res.*, *112*, A06225, doi:10.1029/2007JA012260.

Tsyganenko, N. A., H. J. Singer, and J. C. Kasper (2003), Storm-time distortion of the inner magnetosphere: How severe can it get?, *J. Geophys. Res.*, *108*(A5), 1209, doi:10.1029/2002JA009808.

Zaharia, S., M. F. Thomsen, J. Birn, M. H. Denton, V. K. Jordanova, and C. Z. Cheng (2005), Effect of storm-time plasma pressure on the magnetic field in the inner magnetosphere, *Geophys. Res. Lett.*, *32*, L03102, doi:10.1029/2004GL021491.

Zaharia, S., V. K. Jordanova, M. F. Thomsen, and G. D. Reeves (2006), Self-consistent modeling of magnetic fields and plasmas in the inner magnetosphere: Application to a geomagnetic storm, *J. Geophys. Res.*, *111*, A11S14, doi:10.1029/2006JA011619.